ACS Catalysis

pubs.acs.org/acscatalysis
Research Article

Expanding the Reaction Network of Ethylene Epoxidation on Partially Oxidized Silver Catalysts

Adhika Setiawan, Tiancheng Pu, Israel E. Wachs,* and Srinivas Rangarajan*

Cite This: ACS Catal. 2024, 14, 17880−17892
Read Online

ACCESS | Metrics & More | Article Recommendations | Supporting Information

ABSTRACT: An extended microkinetic model (MKM) for the selective oxidation of ethylene to ethylene oxide (EO) is presented, based on an oxidic representation of the silver (Ag) surface, namely, the p(4 × 4) oxidic reconstruction of the Ag(111) phase to mimic the significant oxygen coverage under reaction conditions, as is evidenced by recent operando spectroscopic studies. The MKM features three pathways each for producing either ethylene oxide (EO) or carbon dioxide (CO_2), including the common intermediate or oxometallacycle (OMC) pathway, an atomic oxygen pathway, as well as pathways centered around the role of a diatomic oxygen species occupying an oxygen vacancy (O_2/O*). The MKM uses a composite set of experimental and density functional theory (DFT) kinetic parameters, which is further optimized and trained on experimental reaction data. A multistart ensemble approach was used to ensure a thorough sampling of the solution space, and a closer analysis was performed on the best-performing, physically meaningful solution. In agreement with published DFT data, the optimized MKM observed that the OMC pathway heavily favors the total combustion pathway and alone is insufficient in explaining the ∼50% EO selectivity commonly reported. Furthermore, it confirmed the pivotal role of the O_2/O* species in the flux-carrying pathways for EO production. The MKM additionally highlights the fluctuating nature of the catalyst surface, in that the proportion of metallic to oxidic phase changes according to the reaction conditions, accordingly resulting in kinetic implications.

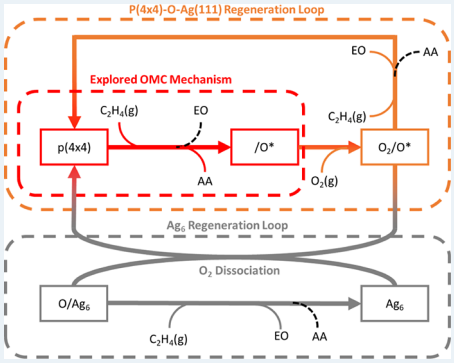

KEYWORDS: *ethylene, oxidation, ethylene oxide, silver, microkinetic modeling, density functional theory*

INTRODUCTION

The selective oxidation of ethylene (C_2H_4) to ethylene oxide (EO) is a relatively mature industrial process producing a pivotal upstream commodity chemical, typically relying on the use of silver (Ag) catalysts,[1−3] heavily modified by promoters such as chlorine, cesium, and rhenium to enhance the desired partial oxidation pathway and limit the total combustion of C_2H_4.

In terms of the mechanism of the EO reaction system, it is generally accepted that there is a common key intermediate in the production of the two main reaction products, EO and carbon dioxide (CO_2), representing the partial and total oxidation pathways, respectively. Following early mechanistic studies by Grant and Lambert,[4,5] which feature the complete decoupling of the partial and total combustion pathways, Linic and Barteau[6] determined, through a series of experiments investigating the reverse reaction of EO adsorption on a Ag(111) single crystal under ultrahigh vacuum (UHV) conditions, that the likely structure of a reaction intermediate is an oxometallacycle (OMC). This species is commonly accepted as the common intermediate for this chemistry[7−13] and is further supported by the experimental evidence of similar magnitudes of apparent activation energies (E_A) and orders of reaction with respect to both reactants (n_{O_2}, $n_{C_2H_4}$).[3,14−16] Building upon this, several kinetic and microkinetic modeling (MKM) studies have been performed, focusing on this OMC-based mechanism. Notably, Linic and Barteau proposed a reaction coordinate for an OMC-based EO synthesis on Ag(111).[12] Building upon this, Stegelmann et al.[17] presented an extension to the prior MKM by including a pathway to produce acetaldehyde (AA) (as a precursor for CO_2) from the common OMC intermediate, as well as an additional decoupled pathway for direct total combustion of C_2H_4. Huš and Hellman proposed a common intermediate model sans the additional direct combustion pathway, and instead treated AA as a desorbing gaseous product, but extended the analysis with a kinetic Monte Carlo (kMC) model for more single-crystal surfaces (Ag(111), Ag(110), Ag(100)).[9]

While the mechanistic studies above are mainly focused on the commonly stable and abundant FCC phases of the Ag catalyst, surface science and spectroscopic studies[18−23] suggest that in the highly oxidizing environment of epoxidation

Received: July 29, 2024
Revised: November 4, 2024
Accepted: November 6, 2024
Published: November 19, 2024

https://doi.org/10.1021/acscatal.4c04521
ACS Catal. 2024, 14, 17880−17892

reactions, the Ag surface is not completely metallic. Xu et al. also demonstrated in their DFT study[24] that the presence of subsurface oxygen atoms on an Ag(111) facet results in appreciable energetic shifts that translate to significant implications when choosing a purely metallic Ag surface as the catalyst model. These observations have motivated the increasing consideration of partially and fully oxidized models of the Ag catalyst. These include the $Ag_2O(001)$ facet studied by Özbek et al.[25,26] looking into the importance of the oxygen vacancies, the O−Ag−O oxide trilayer models featured in studies by Li, Stampfl, and Scheffler,[18] and the partially oxidized Ag featuring Ag_6 or Ag_{10} triangular building blocks in the study by Besenbacher et al.[19] More recently, the trend continues with the study of "hybrid oxygen structures" by Tang et al.[27] and Liu et al.[28] which identified many forms of reactive oxygen species in the EO reaction system.

The apparent complexity of the reaction system then led to alternative studies that deviated from the mainstream OMC-based mechanism. This includes works exploring the mechanism on oxidized surfaces such as the "direct" EO pathway on bulk Ag oxide featured in the works of van Santen et al.,[29] in which EO is produced without the formation of an OMC-like intermediate on Ag_2O surfaces, or translations of the OMC-based mechanism onto partially oxidized Ag(111) and Ag(110) surfaces in the DFT work of Jones et al.[30] Harris et al.[31] showed a non-OMC-based kinetic model for ethylene oxidation on chlorine (Cl) promoted metallic Ag, which was able to account for the changing EO selectivity and ethylene consumption reaction orders with changing Cl content. Most recently, Liu et al.[32] published an MKM for the reaction system that involves both an OMC-based Langmuir−Hinshelwood (LH) and an Eley−Rideal (ER) epoxidation mechanisms and importantly highlights that ethylene epoxidation can proceed on various configurations of the Ag catalyst surface with differing extents of oxidation.

In recognition of the breadth of varied interpretations seen in the literature, two key questions arise: 1) Is it sufficient to model the Ag catalyst using metallic models, or is there a need to consider more complicated partially/fully oxidized models? and 2) Is the framework of the OMC-based mechanism sufficient not only in providing a model for the reaction network but also, more importantly, in capturing the kinetics and the molecular-level details of the reaction? Or is it necessary to also consider alternative pathways? The current study attempts to address these questions using a combination of DFT, kinetics experiments, and microkinetic modeling, with insights leveraged from our prior spectroscopic studies.[21,33] In particular, we calibrate our models to ensure we have quantitative and qualitative parity with the experiments, allowing us to make reliable predictions of the reaction pathways and surface coverages.

METHODS

Density Functional Theory (DFT). All DFT calculations were carried out using the Vienna Ab-initio Simulation Package (VASP) software.[34−37] In all of the cases, a 4 × 4 slab model with periodic boundary conditions is used, consisting of four layers with the bottom two layers fixed to simulate the difference in the dynamic nature of the surface region compared to the bulk phase. A 15 Å vacuum is included perpendicular to the surface. Calculations for gas-phase molecules are done in a large cubic unit cell to simulate the individual gas molecules in a vacuum with minimal interunit cell interactions. All of the calculations are done using the projector augmented wave (PAW) potentials with generalized gradient approximation (GGA) along with the Perdew−Burke−Ernzerhof (PBE) exchange-correlation functional[38] with a dDsC dispersion correction.[39−41] An energy cutoff of 500 eV was used with a self-consistent field (SCF) convergence criterion of 10^{-6} eV and a force-convergence criterion of 0.02 eV/Å. Methfessel−Paxton smearing was used with a spread of 0.1 eV, and a Monkhorst−Pack 5 × 5 × 1 K-point sampling was used. The chosen settings for these parameters were based on an initial benchmarking study. Spin-polarized calculations were used for all cases. For the sampling of transition states, nudged elastic band (NEB)[42−44] analyses were performed using seven intermediate images, which were carried out up to a force convergence criterion of 0.5 eV/Å, with a refinement run using the climbing-image nudged elastic band (CI-NEB)[45,46] method using a tighter force convergence criterion of 0.1 eV/Å.

Microkinetic Modeling. A continuous stirred tank reactor (CSTR)-based microkinetic model (MKM) is constructed to represent the reaction system as a differential algebraic equation (DAE) network. The CSTR model is a reasonable choice for modeling low single-pass conversion (≤15%) heterogeneous catalytic reactions. The single-site model can be written in the following form:

$$\frac{d\theta_i}{dt} = \sum_{j\in J} \nu_{ij} r_j \; i \in I^S \tag{1}$$

$$1 = \sum_{i\in I^S} \theta_i d_i + \theta^* \tag{2}$$

$$r_j = k_j \prod_{i\in I_j^{G,rxt}} [P_i]^{|\nu_{ij}|} \prod_{i\in I_j^{S,rxt}} [\theta_i]^{|\nu_{ij}|} [\theta^*]^{|\nu_j^*|} \tag{3}$$

Here, i and j are the indices over the total of I species and J reactants, respectively. k_j is the Arrhenius reaction rate constant for reaction j. θ_i is the mean-field surface coverage of species i with denticity d_i, while θ^* represents the free site coverage. ν_{ij} is the stoichiometric coefficient of species i in reaction j, while ν_j^* represents the stoichiometric coefficients specifically for the free sites. Superscripts over the entire set of species and reactions represent subsets thereof. The superscripts G and S represent the subset of only gaseous and only surface species, respectively. A more complete formulation of the MKM is included in Sections S1−S3. The MKM is implemented in Python 2.7 with CVODES from the SUNDIALS suite[47,48] as the integrator. The extended formulation of the microkinetic model is included in Section S1. To ensure parity with experimental models, deviations from the kinetic parameters can be introduced and optimized in the parameter optimization workflow below.

Parameter Optimization Workflow. The generalized procedure for parameter optimization is summarized in Figure 1. The experimental data set is used to both initialize the reaction conditions over which the model is trained and evaluate the accuracy of the model-predicted turnover frequency (TOF) values. The TOF is defined as the number of reaction events occurring per unit time normalized to the number of active catalytic sites. Deviations from the kinetic parameters of each reaction step and thermodynamic parameters of each species in the MKM (δE_A and δH_f) serve as the decision variables that are optimized at every iteration of the optimization loop. As noted, the objective chosen for optimization is the root-mean-square error (RMSE) of the model-predicted TOF values relative to

https://doi.org/10.1021/acscatal.4c04521
ACS Catal. 2024, 14, 17880−17892

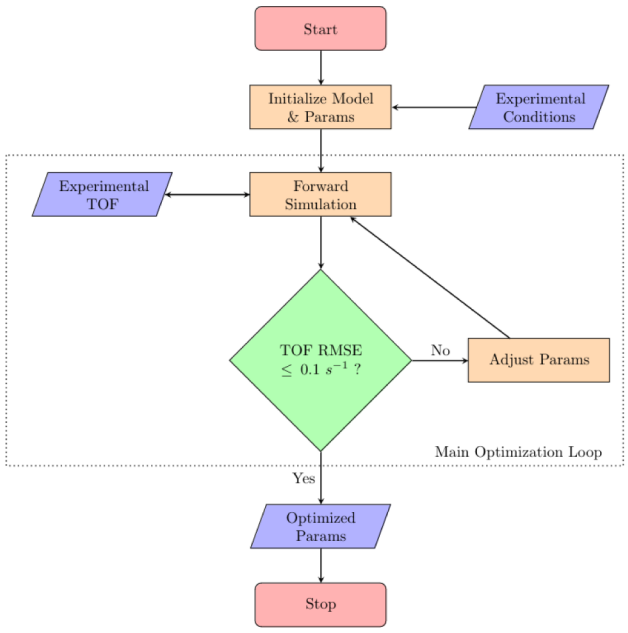

Figure 1. Flowchart of the parameter optimization procedure. Rectangles with rounded corners represent end points, rectangles represent processes, trapezoids represent inputs/outputs, and diamond represents decision points.

their experimental values. Solving the MKM-optimization problem comes with commonly reported challenges:[49−51]

- High degree of nonlinearity due to the stiffness of the optimization problem.
- Strategies should be adopted to minimize issues related to overfitting.
- Thorough coverage of the solution space to compare solutions beyond a particular minimum.

Various strategies have been proposed in tackling stiff optimization problems, including the use of various algorithms like Sensitivity-Supervised Interlock Algorithm (SSIA),[52] Particle swarm optimization and modified NEWton's method Coupling System (PNEWCS),[50,51] and Reversibility Iteration Method (RIM).[53] In our case, an automatic differentiation (AD) algorithm was found to be capable of tackling the optimization problem. To minimize possible overfitting issues, an *L2* regularization term was included in the optimization loss function to favor smaller parameter shifts away from the initial DFT values. The *L2* regularization term was ensured to be ≤∼5% of the objective value. Finally, to ensure ample coverage of the solution space, a multistart approach is used, which results in an ensemble of similar models, from which the best-performing model is selected for further analysis. The sequential and multistart optimization procedure is implemented in Python 2.7 with IPOPT[54] under CasADi[55] for the optimization. The individual instances in the multistart optimization are run in parallel with an RNG-randomized seed for every batch of 8000 instances, each of which was randomized following a uniform random distribution within defined bounds. Detailed formulations of the MKM and the parameter optimization procedure are included in Sections S1−S4.

Experimental Data. *Materials.* The α-Al_2O_3 support was purchased from CeramTec. Silver oxalate (≥99%) was prepared by Scientific Design Inc. Ethylene diamine was purchased from JT Baker (≥98%). NH_4Cl was purchased from Sigma-Aldrich (ACS Reagent Plus, ≥99%). The gas supplies (Ar balance, 40% O_2/He, C_2H_4 (99.99%), and CO_2 (99.99%)) for steady-state ethylene oxidation experiments were purchased from Praxair.

Catalyst Preparation. The supported Ag/α-Al_2O_3 catalyst was synthesized with Ag loading of ∼16 wt%. The Ag/α-Al_2O_3 catalyst was prepared using the standard incipient-wetness impregnation method by using silver oxalate as the precursor. The Ag complex solution was prepared by mixing silver oxalate, ethylene diamine, and deionized water at a mass ratio of 1:0.5:0.5. The desired amount of solution was mixed with α-Al_2O_3 support and stirred for 30 min. The mixture was allowed to dry at 90 °C overnight before being calcined at 450 °C in N_2 for 45 min. CO temperature-programmed reduction (CO-TPR) is used to determine the number of active sites and for catalyst reducibility assessments.

Steady-State Kinetics Measurements. For steady-state ethylene oxidation in a fixed-bed reactor, 0.5 g of catalyst (40−60 mesh) was used. The reaction mixture nominally consisted of 25% C_2H_4, 7% O_2, and 2% CO_2 balanced by He at atmospheric pressure. The flows were adjusted with a Brooks 5850E mass flow controller (MFC) to the desired composition and passed over the catalyst (at nominal WHSV= 6000 $\frac{mL}{gcat \cdot h}$). The catalyst was loaded into a microflow quartz reactor (3 mm i.d.), and reactions were performed at 170−220 °C in a vertical tube furnace system. Before the steady-state kinetics test, the catalyst was first oxidatively dehydrated in 5% O_2/Ar at 100 °C for 1 h and then preconditioned by reaction with 8% C_2H_4, 4% O_2, and 4% CO_2 at 240 °C for 3 h. The conversion of C_2H_4 and the formation of EO were quantified with an Agilent 6890 gas chromatograph with a Poraplot Q column equipped with a flame ionization detector (FID) and a thermal conductivity detector (TCD). The products, EO and CO_2, were monitored by FID and TCD detectors, respectively. The conversion of C_2H_4 is calculated from the carbon balance. In order to determine the reaction orders of EO and CO_2 formation over the supported Ag/α-Al_2O_3 catalyst with respect to C_2H_4 and O_2, the temperature was held constant at 190 °C for Ag/α-Al_2O_3 to ensure comparable C_2H_4 conversion at ∼5%. The C_2H_4 feed was adjusted from 10% to 40% while the O_2 feed was maintained at 7% for the C_2H_4 reaction order determination. The O_2 feed was adjusted from 7% to 30% while the C_2H_4 feed was maintained at 12% for the determination of the order of the O_2 reaction. For each data point, the system was allowed to run for at least 30 min prior to data collection to ensure steady-state operation.

RESULTS AND DISCUSSION

Feasibility of Bypassing the OMC Intermediate. A key initial step involves the assessment of the feasibility (from a reaction kinetics perspective) of considering an alternative pathway to the OMC intermediate in the first place. The previously cited MKM by Stegelmann et al.[17] was chosen as the control model as the mechanism featured in the model is centered around the OMC intermediate, and it also features an interesting usage of the /O* species nomenclature, representing "some kind of surface oxide site". In the original Stegelmann model, the kinetic parameters for the forward and backward reactions (pre-exponential factors A_i and transition state enthalpy $\Delta H_i^{\ddagger}$) were defined independently from each other, which does not inherently ensure thermodynamic consistency[56] in the formulation. Therefore, the first step involves implementing thermodynamic consistency by reformulating the Stegelmann model in terms of the forward activation barrier in each

https://doi.org/10.1021/acscatal.4c04521
ACS Catal. 2024, 14, 17880−17892

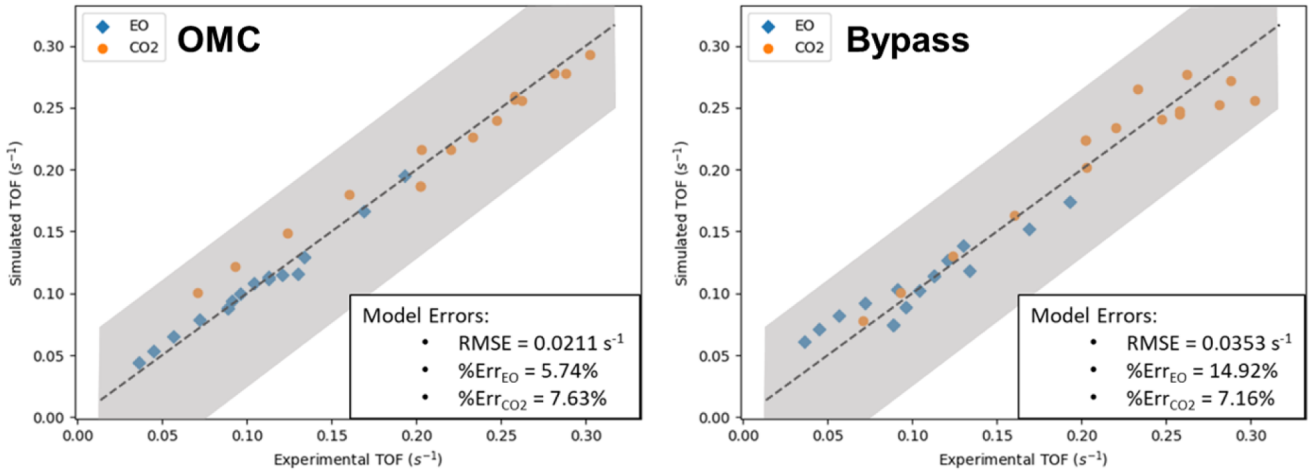

Figure 2. Parity plots comparing the simulated and experimental TOF values from two different types of models: an OMC-based model (**Left**) and a non-OMC-based model (**Right**). The reported RMSE and percentage error values are based on TOF. The gray shaded region represents experimental data uncertainty.

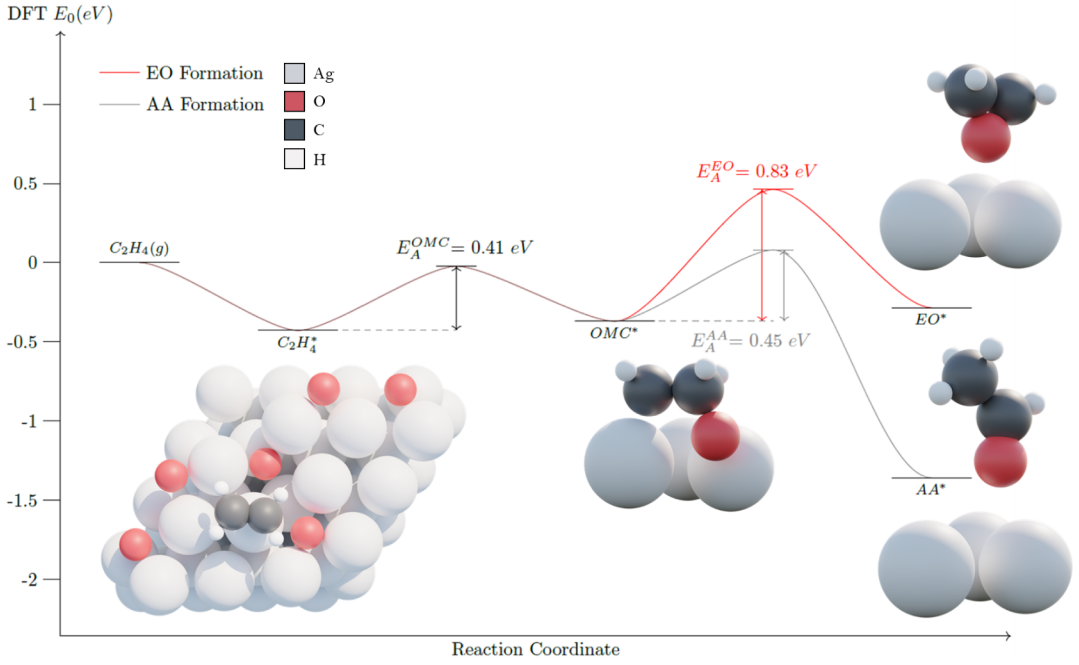

Figure 3. 2D potential energy diagram along the reaction coordinate of the OMC-based partial oxidation mechanism. All of the states are presented relative to the initial state, and the reported E_A values correspond to their adjacent double-sided arrows. Atomic representations of the different intermediates are included (from left to right): top view of C_2H_4*, side view of the truncated OMC* structure, and side views of the truncated EO* and AA* intermediates.

elementary step used in the original model (E_A) and the formation energy of each of the surface species involved (H_f). Additionally, thermodynamic consistency constraints were applied (Section S2), and the parameters for the reverse elementary reactions were defined in relation to their forward counterparts via the equilibrium constant. To ensure that the reformulated model stays consistent with its original reference, the parameter optimization procedure described earlier was performed with the deviations from the aforementioned new parameters (δE_A and δH_f) as decision variables, with the additional constraint that the post-optimization kinetic parameters stay as close as possible (activation barriers deviating no more than ~10 kJ/mol) to the reference Stegelmann model.

Following the implementation of thermodynamic consistency, the feasibility of bypassing the OMC intermediate was assessed. A nonelementary bypass reaction that allows for the formation of EO *without* the explicit formation of the OMC intermediate was added to the MKM, after which a parametric reoptimization was performed to generate a second pool of different types of models (again, with δE_A and δH_f as decision variables and TOF RMSE as the optimization objective), particularly ones in which the reaction flux does *not* go through the formation of the OMC intermediate. The training data for parameter optimization include the following reaction condition ranges: T = 443−468 K, $P_{C_2H_4}$ = 0.13−0.30 atm, P_{O_2} = 0.07−0.2 atm, P_{CO_2} = 0.02 atm.

https://doi.org/10.1021/acscatal.4c04521
ACS Catal. 2024, 14, 17880−17892

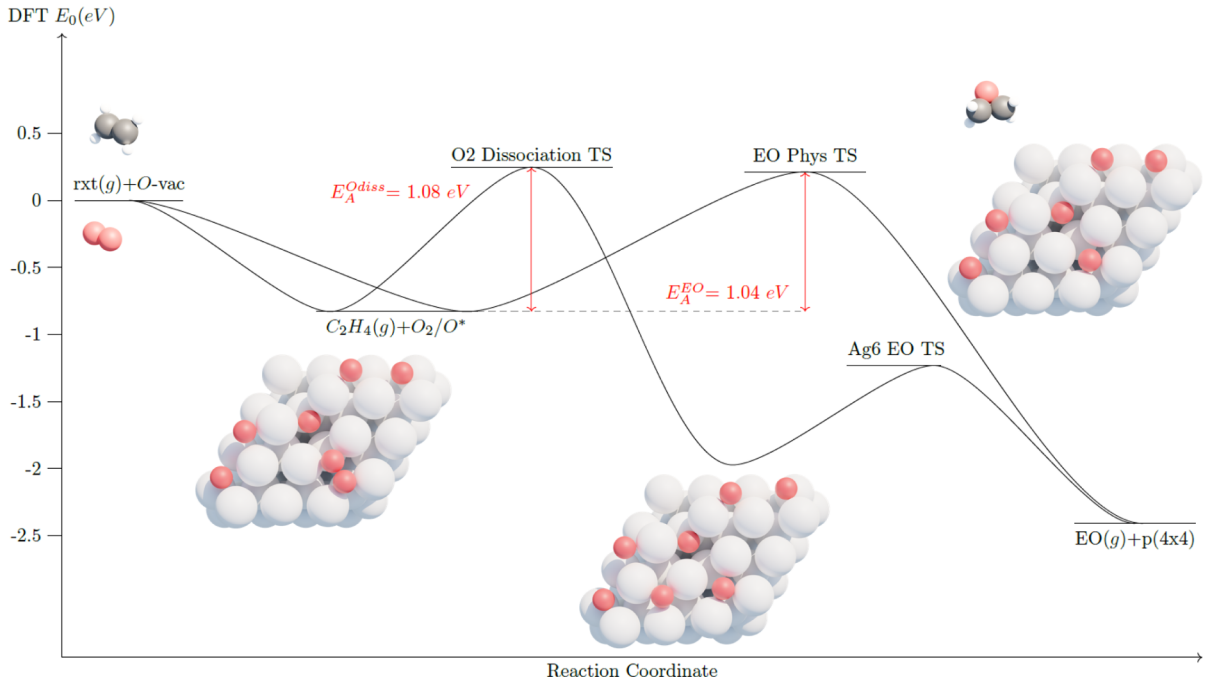

Figure 4. 2D potential energy diagram along the reaction coordinate of a direct partial oxidation mechanism. All of the states are presented relative to the initial state, and the reported E_A values correspond to their adjacent double-sided arrows. Atomic representations of the different intermediates are included (from left to right): reactant gases (rxt(g)), top view of O_2/O*, top view of O/Ag_6, and the regenerated p(4 × 4)-O-Ag(111) surface with the EO product.

Parity plots of the best models from both runs are shown in Figure 2. Clearly, both models perform well, and importantly, all of the TOF values fall within the experimental uncertainty of the training data set. Statistically speaking, therefore, the non-OMC model performs, as well as the OMC model, in reproducing the experimental data. Additionally, the predicted steady-state surface coverage of the non-OMC-based model (Figure S.5) points to a high coverage of O* and O/O*, which further motivates the investigation toward partially oxidized Ag surfaces. The next sections detail our DFT-based exploration of the atomic picture of the common intermediate mechanism and the "bypass" mentioned above in the context of a partially oxidized Ag surface.

Common-Intermediate Mechanism on a Partially Oxidized Surface. Previous studies[28,57] have noted that there exist various known configurations of AgO_x surfaces with different extents of oxidation, and it was additionally confirmed through recent XPS and AP-XPS studies that an Ag catalyst undergoes phase transitions toward an oxidized Ag phase under reaction conditions.[21,58] For the scope of this study, the p(4 × 4)-O-Ag(111) partially oxidized surface was chosen as the model catalyst to represent a partially oxidized Ag catalyst due to its stability and relatively ordered structure with a Ag_2O stoichiometry.

The OMC-based mechanism[12] was first studied on the p(4 × 4)-O-Ag(111) surface using DFT calculations. The results show that, following an initial activation of the ethylene double bond via adsorption onto a $Ag^{\delta+}$ site[5,59−61] (charge analysis included in Table S.6), C_2H_4* then reacts with an O atom that is *part of* the unmodified p(4 × 4)-O-Ag(111) surface to form the OMC intermediate, which then forms either EO or AA. In agreement with previously reported studies,[25,30,62] multiple pathways of forming either EO or AA were considered depending on slight configurational changes in the transition state and/or the adsorbed product state. Among them, the most energetically favorable ones for EO and AA are shown in Figure 3. There is a mismatch between the expected ∼50% EO selectivity for unpromoted Ag catalysts[3,8,63−65] and apparent activation energy (E_A) difference obtained from DFT (0.38 eV), which clearly favors the total combustion pathway. It is likely that a common-intermediate mechanism, while relevant, does not comprehensively capture the key portions of the EO reaction system. An extended set of reactions may be necessary to represent the mechanism on a partially oxidized surface.

Beyond the First Oxidation. One key difference between the metallic and oxide surfaces of Ag is the generation of oxygen vacancies. On a metallic Ag surface, the oxidant is an adsorbed oxygen. On the oxide surface, the oxygen atom that is *part of* the oxidized surface can react with ethylene, in which case an oxygen vacancy is created after the initial OMC-like mechanism (Figure S.9).

Borrowing the nomenclature used in the model by Stegelmann et al.,[17] the naming convention O/O* will henceforth be used to describe the oxygen atoms that are part of the unmodified p(4 × 4)-O-Ag(111) surface, and thus, /O* will be used to represent the oxygen vacancy site. Other adsorbate nomenclature follows similar logic, e.g., O_2/O* represents a dioxygen molecule adsorbed at an oxygen vacancy site.

The creation of a vacancy site, /O*, opens up new reaction steps not relevant to the metallic surface. Notably, the $O_2(g)$ molecules can adsorb *into* the oxygen vacancy, forming an O_2/O* species. There are ongoing discussions on similar dioxygen species under different names like "hybrid dioxygen", or simply, a dioxygen occupying the vacancy that was previously occupied by an atomic oxygen.[28,66−69] Studies that looked into lower-symmetry representations of the silver oxide phase similarly identified the adsorbed dioxygen species as occupying an

https://doi.org/10.1021/acscatal.4c04521
ACS Catal. 2024, 14, 17880−17892

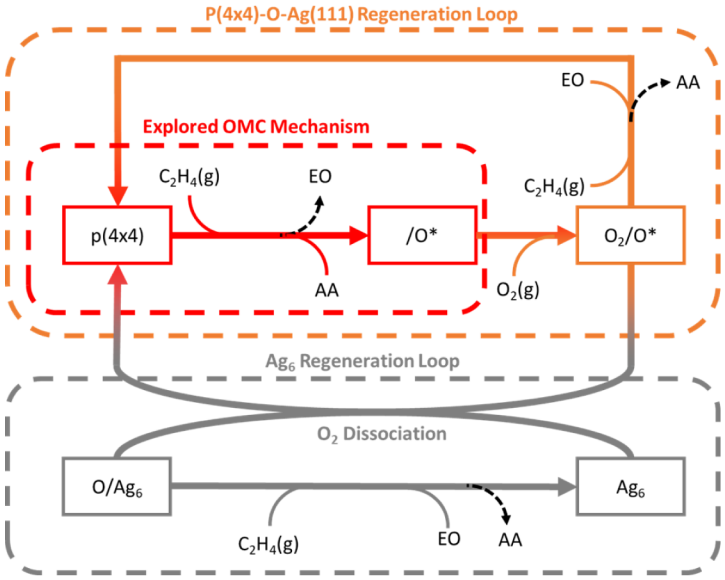

$O_2(g) + * \rightleftharpoons O_2^*$	O_2 Ads $r1$
$O_2^* + * \rightleftharpoons 2\,O^*$	O_2 Diss $r2$
$O_2(g) + 2\,O^* \rightleftharpoons 2\,O/O^*$	p4x4 Form $r3$
$C_2H_4^* + O/O^* \rightleftharpoons CH_2CH_2O/O^* + *$	OMC Form $r4$
$C_2H_4O(g) + /O^* \rightleftharpoons C_2H_4O/O^*$	EO Ads Vac $r5$
$CH_2CH_2O/O^* \rightleftharpoons C_2H_4O/O^*$	OMC to EO $r6$
$CH_2CH_2O/O^* \rightleftharpoons CH_3CHO/O^*$	OMC to AA $r7$
$CH_3CHO^* + 7\,O^* \rightleftharpoons 2\,CO_2^* + 4\,OH^* + 2*$	AA Combust $r8$
$C_2H_4(g) + * \rightleftharpoons C_2H_4^*$	C_2 Ads $r9$
$C_2H_4/O^* + O^* \rightleftharpoons CH_2CHOH/O^* + *$	C_2 Combust $r10$
$CH_2CHOH/O^* + O^* \rightleftharpoons CH_2CHO/O^* + OH^*$	C_2 Combust $r11$
$CH_2CHO/O^* + 5\,O^* \rightleftharpoons 2\,CO_2^* + 3\,OH^* + *$	C_2 Combust $r12$
$2\,OH^* + * \rightleftharpoons H_2O^* + O^*$	H_2O Form $r13$
$CO_2^* + * \rightleftharpoons CO_2(g) + *$	CO_2 Des $r14$
$H_2O^* + * \rightleftharpoons H_2O(g) + *$	H_2O Des $r15$
$C_2H_4^* + O^* \rightleftharpoons C_2H_4O^* + *$	EO Form Ag6 $r16$
$C_2H_4O(g) + * \rightleftharpoons C_2H_4O^*$	EO Ads Ag6 $r17$
$O_2(g) + /O^* \rightleftharpoons O_2/O^*$	O_2 Ads vac $r18$
$C_2H_4(g) + O_2/O^* \rightleftharpoons O/O^* + C_2H_4O(g)$	Direct EO Form $r19$
$C_2H_4(g) + O_2/O^* + * \rightleftharpoons O/O^* + CH_3CHO^*$	dOMC AA Form $r20$
$CH_3CHO/O^* + * \rightleftharpoons CH_3CHO^* + /O^*$	AA Diff $r21$
$O_2/O^* + * \rightleftharpoons O^* + O/O^*$	O_2 Diss $r22$

Figure 5. Left: Schematic illustration of the extended reaction network, showing the three oxidation pathways in red, orange, and gray. **Right**: An extended reaction network was used for the selective oxidation of ethylene. Steps shaded in gray are taken verbatim from the referenced MKM by Stegelmann et al.,[17] the steps shaded in blue have their representation altered with the new usage of the O/O* nomenclature, and steps shaded in red are added after DFT exploration.

"oxygen vacancy" typically with vibrational mode frequencies at around 750−800 cm^{-1} as opposed to surface-adsorbed O_2 vibrating at the 1050−1100 cm^{-1} range.[28,70,71] Our previous study[21] additionally reported that slight rotational configuration changes of the O−O bond axis relative to the surface could result in DFT energy differences upwards of 70 kJ/mol and vibrational frequency shifts upwards of 200 cm^{-1}. In consideration of these differences and for the sake of consistency, mentions of the O_2/O* species in this study will henceforth refer to one in which the O−O bond axis is parallel to the surface (Figure S.10) as it is the most stable out of the pool of sampled configurations. Our DFT calculations additionally observed that the transitions between the different rotational configurations are unactivated, and thus, thermodynamics will drive the different configurations toward the most stable parallel configuration. The parallel configuration also exhibits a vibrational frequency most closely associated with the active oxygen species in previous Raman spectroscopy studies of the reaction system.[21]

As illustrated in Figure 4, once the O_2/O* species is formed, it can dissociate to regenerate the initial O/O* site while depositing an O atom at the adjacent 3-fold Ag site (O/Ag_6), which could then react with C_2H_4 to form EO (labeled as "Ag_6 EO" pathway), or a gaseous C_2H_4 molecule can physisorb onto the O_2/O* species and react with one of its O atoms in a partial oxidation step without the need to form OMC (labeled as the "EO Phys" pathway for the way the reactant C_2H_4 directly physisorbs onto the reacting oxygen); either outcome results in the regeneration of the initial p(4 × 4)-O-Ag(111) surface, completing the catalytic cycle. As the apparent barriers for these two partial oxidation steps are similar in magnitude, both reactions are included in the MKM in this study. To reiterate, the p(4 × 4)-O-Ag(111) is chosen as a model catalyst to conceptually assess the general reaction mechanism of ethylene epoxidation on partially oxidized Ag surfaces. This model was also chosen as it features multiple oxygen-based species that can react as the oxidant for ethylene: molecular adsorbate (O_2*), atomic adsorbate (O*), atomic oxygen below the top Ag layer (O/O*), and molecular oxygen below the top Ag layer (O_2/O*). In reality, a mixture of oxidized Ag phases and oxygen species can exist under the oxidizing epoxidation conditions,[27,28,57,72−75] and the observed experimental kinetics will be the compound effects of these mixed conditions, even among similar types of oxygen species, but the p(4 × 4)-O-Ag(111) model is utilized here as a general representation. Furthermore, in this representation, the /O* free site serves a key role in maintaining the site economy between the different oxygen species, as well as a key precursor to the active O_2/O* species. The details of C_2H_4 oxidation via physisorption onto a singlet oxygen are discussed in Section S6, and a discussion on the different total combustion pathways considered is included in Section S7.

Parameter Optimization of an Extended MKM. The new pathways for ethylene oxidation identified using DFT were added to the existing OMC-based model to form the extended reaction network. Additional steps explored via DFT are added to the Stegelmann model as additional pathways shaded in red in Figure 5 (**Right**), and the steps highlighted in blue now explicitly represent reactions on a p(4 × 4)-O-Ag(111) surface. As illustrated in Figure 5 (**Left**), this extended model features three main pathways for producing EO, with an alternate path for the Ag_6 pathway depending on the source of oxygen:

- OMC-based Pathway: *r3* → *r4* → *r6* → *r5*
- Vacancy-based Pathway: *r18* → *r19*
- Ag_6 Pathway: *r18* → *r22* → *r16* → *r17*
- Ag_6 Pathway-Alt: *r1* → *r2* → *r16* → *r17*

The critical difference here is that, with the modification in nomenclature, the kinetic parameters of each step need to be redefined accordingly, except for existing steps occurring on the metallic-like portions of the surface. In other words, the steps in blue have their parameters updated using the DFT data for the equivalent reactions on a p(4 × 4)-O-Ag(111) surface, while the adsorption and combustion steps in gray remain unaltered. For the remaining steps in red, the kinetic parameters are derived from additional DFT calculations. Subsequently, a parameter

https://doi.org/10.1021/acscatal.4c04521
ACS Catal. 2024, 14, 17880−17892

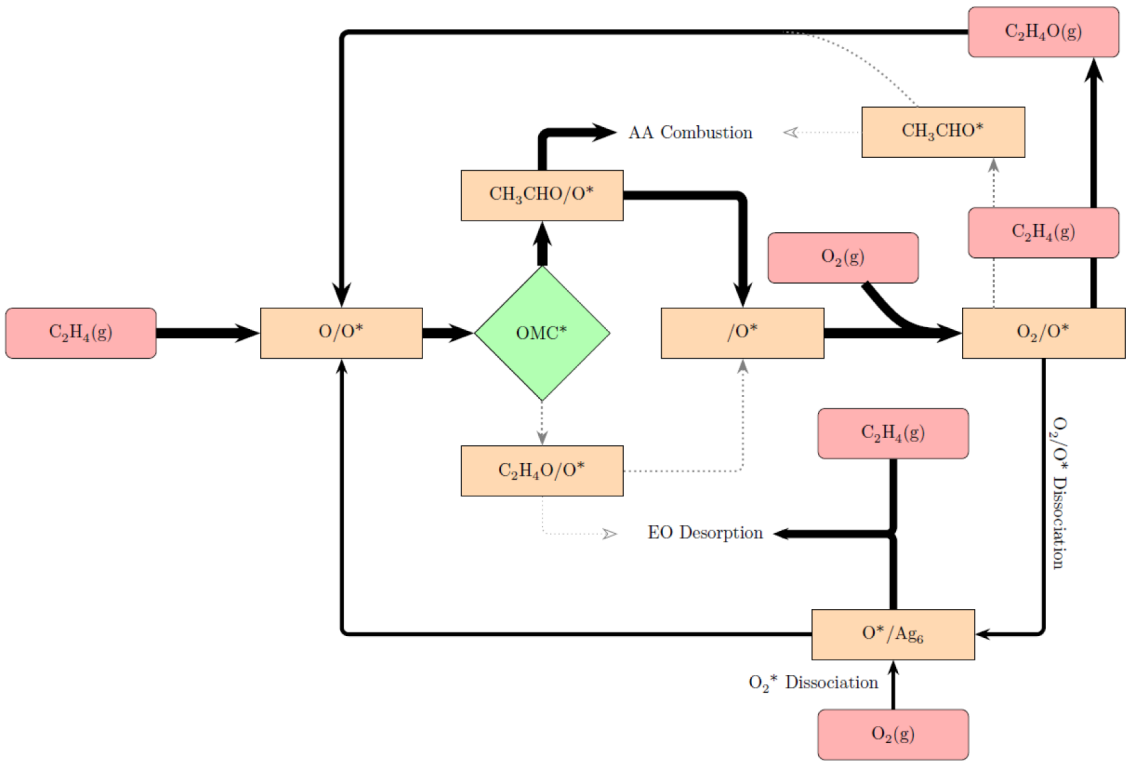

Figure 6. Reaction flux diagram showing the main EO generation pathways. The thickness of the arrows indicates the magnitude of fluxes, and gray arrows indicate fluxes that are at least two orders of magnitude smaller than the rest. Pastel red rectangles indicate gaseous species. Pastel orange rectangles indicate surface intermediates. The pastel green diamond represents an OMC common intermediate. Steps related to the combustion pathways are not included.

reoptimization procedure (Section S2) was carried out on the kinetic parameters to minimize the model-predicted TOF RMSE. With the DFT-derived kinetic parameters as a starting point, additional rounds of multistart optimization procedures were performed, resulting in an ensemble of models. To maintain relevance to the initial guess of the kinetic parameters, energetic deviations during the parameter optimization steps are maintained to not exceed ±35 kJ/mol, with an overall average in deviation across all parameters of ±15 kJ/mol. Details on the DFT-derived MKM steps are included in Section S8.

Additionally, the binding energy (BE) of molecular O_2 on a metallic Ag site is a key point of discussion. Various BE values have been reported,[9,24,76] ranging from DFT-based values of ∼0.15 eV for O_2*/Ag(111) (uncorrected for the typical 0.3−0.4 eV $O_2(g)$ DFT errors), followed by stronger adsorption on more open facets and/or with higher coverage of subsurface oxygen (O_{sub}), up to ∼1.1 eV for O_2 adsorption on Ag(111) with 1 ML coverage of O_{sub}. The Stegelmann model uses a BE value of 44.5 kJ/mol, close to the experimental value of 38.5 kJ/mol reported by Campbell, both of which assumed a metallic Ag(111) facet to represent the surface. In this case, however, since a more oxidized surface representation is considered, a higher BE value is expected. For the sake of completeness, three different initial guesses for the BE values were used (40, 70, and 100 kJ/mol), which encompass the full range of reported values when considering the ±35 kJ/mol allowed deviation bounds. Over the series of initial optimization rounds, it was found that the model was able to reproduce the experimental data when the $O_2(g)$ BE is set to 83.9 kJ/mol, which corresponds to the DFT values of O_2*/Ag(111) adsorption with an O_{sub} coverage between 0.5 and 1.0 ML[24] (accounting for the typical 0.3−04 eV $O_2(g)$ DFT errors).

Filtering Physically Meaningful Solutions. The parameter optimization procedure generates a pool of solutions with the main goal of minimizing TOF RMSE, independent of any other nuances in chemical kinetics. Therefore, some solutions achieve very low RMSE values but are not necessarily physically meaningful. To address this, postoptimization solutions are filtered based on the following criteria:

- All reaction orders of both reactants w.r.t. both products are positive.
- Apparent activation energy values must be between 50 and 150 kJ/mol.
- Apparent activation energy values of both main products must be within 25 kJ/mol of each other.

The statistics of the reduced pool of solutions that passed the above filtering process are summarized in Section S5. Note that, in future uses of the model, especially when extended to promoted catalyst training data, the criteria of the filtering process can be adjusted accordingly. Additionally, two general types of solutions exist for the models when the reaction is performed at the following conditions: T = 467.95 K, $P_{C_2H_4}$ = 0.25 atm, P_{O_2} = 0.07 atm, P_{CO_2} = 0.02 atm. These are as follows:

- **Type I**: Solutions in which there is a large coverage of the surface by species unobserved in spectroscopic studies. While these types of solutions were able to reproduce experimental TOF within 5% of the experimental data, they also exhibit unexpectedly large coverages ($\theta \geq 0.1$ ML) of intermediates like vinyl alcohol, acetaldehyde, OH*, and CO_2*, as well as the kinetic significance ($\chi_{RC} \geq 0.1$) of corresponding steps.

https://doi.org/10.1021/acscatal.4c04521
ACS Catal. 2024, 14, 17880−17892

- **Type II**: Solutions in which the direct EO formation via the singlet oxygen (*r19*) is the most rate-controlling at nominal conditions, conversely showing kinetically insignificant steady-state coverages ($\theta \leq 0.05$ ML) of vinyl alcohol, acetaldehyde, other unexpected intermediates, and higher steady-state coverages of oxygen-based species (O*, O_2*, /O*, O/O*, and O_2/O*).

Between the two, solution **Type I** tends to exhibit lower TOF RMSE values, but vinyl alcohol coverage is generally unexpected under experimental reaction conditions. The higher coverage is attributed mainly to how the combustion step *r12* is defined, requiring the simultaneous presence of five distinct instances of O*, which then translates to a probabilistic hurdle in the Arrhenius expression. On the other hand, solution **Type II**, while exhibiting higher TOF RMSE values, makes more physical sense, at least in terms of the expected steady-state coverages. Despite the distinction, most of the qualitative trends are maintained across the solution types. The flux of reactant going through the OMC formation pathway (*r4*) preferentially leads to total combustion products (by several orders of magnitude relative to the production of EO from the OMC), and this reaction serves a key role in maintaining the economy of the vacancy sites/O*. In all of the solutions, the flux-carrying pathways toward EO formation are the direct formation via the singlet oxygen/vacancy-based pathway (*r19*) and the Ag_6 pathway (*r16*), both of which are dependent on the O_2/O* species. In the scope of this study, the parameter optimization procedure is mainly used as a tool to perform a wide search of similar solutions. The detailed analysis of the MKM will be done by focusing on the best-performing individual solution under **Type II**.

Analysis of the Best-Performing Individual Model. *Overall Fits: TOF, Activation Barrier, and Reaction Orders.* Figure 7 shows how the best-performing **Type II** model out of the aforementioned solution pool reproduces the experimental data across a range of experimental conditions. For reference, the reaction flux diagrams of the main EO-producing pathways are included in Figure 6. Following the convention in Table S.5, the experimental data can largely be divided into three subsets, where the varied conditions for each subset are the reaction temperature, oxygen partial pressure (P_{O_2}), and ethylene partial pressure ($P_{C_2H_4}$), respectively. Figure 7 shows that the MKM was able to capture the similar apparent barriers between the two products and reproduce the TOF values, on average, within 20%

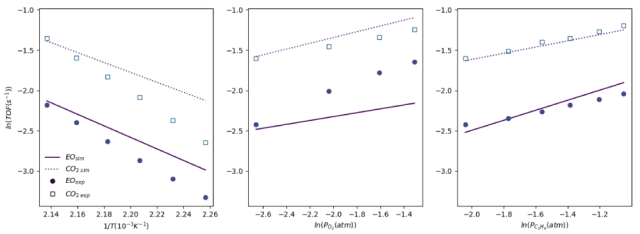

Figure 7. All three subplots share the same *y*-axis. **Left**: Arrhenius plot of EO and CO_2 formation using the extended MKM at the following conditions: T = 443.18−467.95 K, $P_{C_2H_4}$ = 0.25 atm, P_{O_2} = 0.07 atm, P_{CO_2} = 0.02 atm. **Middle**: ln(TOF) of EO and CO_2 as a function of O_2 partial pressure at the following conditions: T = 468 K, $P_{C_2H_4}$ = 0.13 atm, P_{O_2} = 0.07−0.27 atm, P_{CO_2} = 0.02 atm. **Right**: ln(TOF) of EO and CO_2 as a function of C_2H_4 partial pressure at the following conditions: T = 468 K, $P_{C_2H_4}$ = 0.13−0.35 atm, P_{O_2} = 0.07 atm, P_{CO_2} = 0.02 atm.

of the experimental data. Figure 7 (**Left**) shows a better reproduction of the TOF at higher temperatures compared with particularly the three data points at lower temperatures. The dependence of activation barrier heights on the reaction temperature is expected, and more importantly, the 10−20 kJ/mol difference in E_A value for a 25 °C gap between the minimum and maximum temperatures in the training data set is in line with the values reported in the literature.[17] In the context of parameter optimization, the objective of simply minimizing TOF RMSE tends to manifest in earlier/coarser optimization batches, achieving better model fits for the temperature variation data but poorer fits for the data with varied $P_{O_2}/P_{C_2H_4}$, or vice versa. This solution bifurcation is expected as all of the reactant pressure variation data (corresponding to Figure 7 (**Middle** and **Right**)) were taken at a fixed temperature value of 468.15 K, while the temperature variation data (Figure 7 (**Left**)) were taken at a fixed inlet pressure ratio.

Oxidic Surface Ratio, EO Selectivity, and Degree of Rate Control. Beyond the reproduction of TOF values and metrics such as reaction orders, the MKM allows us a closer look into the model-predicted nature of the surface. Figure 8 highlights how two metrics change due to variations in reaction temperature and $P_{O_2}/P_{C_2H_4}$ ratio in the feed. S_{EO} is well understood as the selectivity toward the EO product, while "oxidized ratio" here is the ratio between the sum of oxygen species whose coverages are predicated on the existing coverage of the p(4 × 4)-O-Ag(111) phase, and the sum of oxygen species that can exist readily on either the metallic surface or the metallic portion of the p(4 × 4)-O-Ag(111) phase.

$$\text{Ox. Ratio} = \frac{\Theta_{O/O^*} + \Theta_{O_2/O^*}}{\Theta_{O^*} + \Theta_{O_2^*}} \tag{4}$$

The oxidized ratio provides a measure of how much of the catalyst surface is in the p(4 × 4)-O-Ag(111) phase under reaction conditions, where higher values signify a larger proportion of the partially oxidized phase. Figure 8 (**Left**) shows that in an unchanging feed composition, an increase in reaction temperature corresponds to a quicker consumption of the O_2/O* species via *r19* and *r22*→*r16*, leading to its lower steady-state coverage, accompanied by an increase in S_{EO}. On the one hand, Figure 8 (**Middle**) points to an intuitive result, where increasing the oxygen chemical potential in the system via P_{O_2} leads directly to an increase in the steady-state coverage of the oxide phase. On the other hand, this increase is coupled with a slight decrease in S_{EO}. The increase in oxygen chemical potential should also increase the accessibility toward the "metallic" oxygen-based species, which are more closely associated with the total combustion pathways (*r8*, *r10*−*r13*). The increase in the oxidized ratio suggests that species like O* are more readily consumed relative to O/O* and O_2/O*. Lastly, a relatively mild trend is seen in Figure 8 (**Right**) as the increase in $P_{C_2H_4}$ did not confer a direct effect on the oxygen chemical potential. Figure S.13 shows a different view of Figure 8, where instead of the oxidized ratio, the total sum of the oxygen species is plotted.

$$\text{Tot. Ox.} = \Theta_{/O^*} + \Theta_{O/O^*} + \Theta_{O_2/O^*} + \Theta_{O^*} + \Theta_{O_2^*} \tag{5}$$

Figure S.13 (**Left**) further supports the temperature-based trends, where the O_2/O* species initially covering the surface is gradually depopulated with the increase in reaction rates at higher temperatures, leaving the oxygen vacancy to populate

https://doi.org/10.1021/acscatal.4c04521
ACS Catal. 2024, 14, 17880−17892

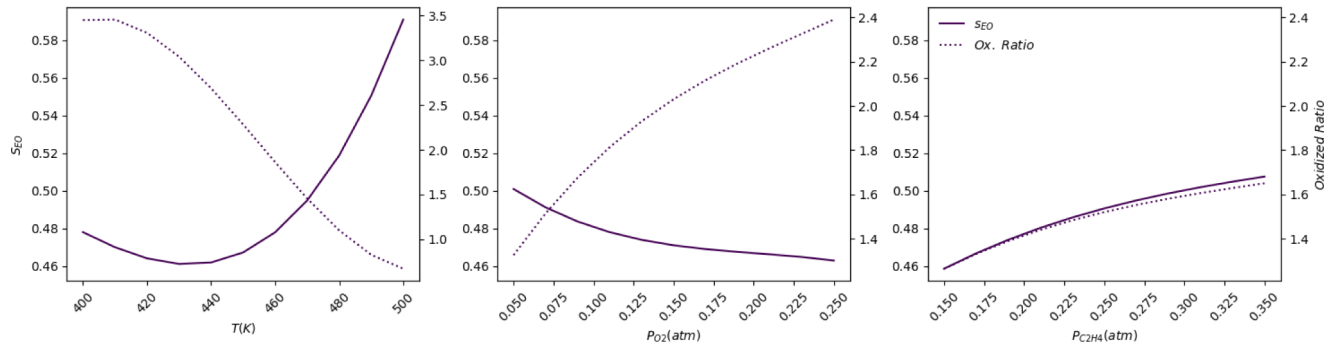

Figure 8. Model predicted EO selectivity (S_{EO}) (**solid**, left axis) and the ratio of oxidized surface (**dotted**, right axis) as a function of reaction temperature, P_{O_2}, and $P_{C_2H_4}$. **Left**: T = 400−490 K, $P_{C_2H_4}$ = 0.25 atm, P_{O_2} = 0.07 atm, P_{CO_2} = 0.02 atm. **Middle**: T = 467.95 K, $P_{C_2H_4}$ = 0.25 atm, P_{O_2} = 0.05−0.25 atm, P_{CO_2} = 0.02 atm. **Right**: T = 467.95 K, $P_{C_2H_4}$ = 0.15−0.35 atm, P_{O_2} = 0.07 atm, P_{CO_2} = 0.02 atm.

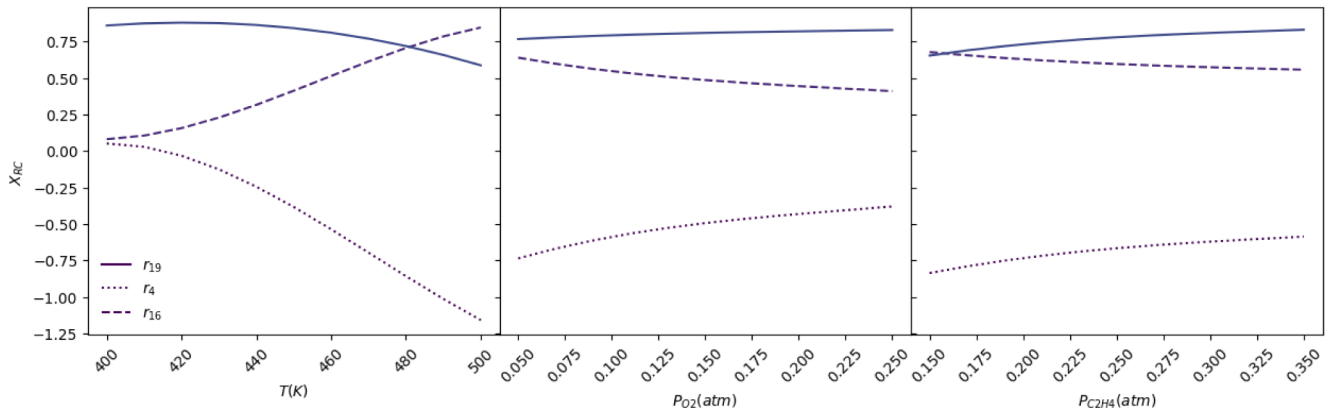

Figure 9. Model predicted degrees of rate control (X_{RC}) of the three main EO-producing pathways as a function of reaction temperature, P_{O_2}, and $P_{C_2H_4}$. **Left**: T = 400−490 K, $P_{C_2H_4}$ = 0.25 atm, P_{O_2} = 0.07 atm, P_{CO_2} = 0.02 atm. **Middle**: T = 467.95 K, $P_{C_2H_4}$ = 0.25 atm, P_{O_2} = 0.05−0.25 atm, P_{CO_2} = 0.02 atm. **Right**: T = 467.95 K, $P_{C_2H_4}$ = 0.15−0.35 atm, P_{O_2} = 0.07 atm, P_{CO_2} = 0.02 atm.

most of the surface. A similar trend was observed in our previous spectroscopic studies,[21,33] where an increase in reaction temperature past ∼400 K was accompanied by a decrease in the ∼800 cm^{-1} Raman band corresponding to O_2/O* and an increase in the ∼300 cm^{-1} band corresponding to the atomic oxygen part of the p(4 × 4)-O-Ag(111) phase in general. Figure S.13 (**Middle**) also corroborates the observation in Figure 8 (**Middle**). An increase in the oxygen chemical potential manifests a direct effect on the equilibrium between the steady-state coverages of O_2/O* and /O*. The same increase in potential is counterintuitively reflected in the static coverage trends of the "metallic" oxygen species, suggesting the faster consumption of O* via combustion pathways, therefore leading to a decrease in S_{EO}. Finally, the mild effect of $P_{C_2H_4}$ in Figure S.13 (**Right**) similarly results in the mild trends in Figure 8 (**Right**).

Furthermore, consistent with recent discussions on the active oxygen species,[33,58] the model identifies O_2/O* as the active oxygen species, maintaining a low steady-state coverage at high enough temperatures as it is being quickly consumed upon generation. As mentioned, across the range of experimental conditions, the reactant flux toward the production of EO is carried by pathways dependent on O_2/O*: the vacancy-based pathway (*r19*) and the Ag_6 pathway (*r16*) via O_2/O* dissociation (*r22*).

Controlling Pathways at Different Regimes. In line with the coverage trends in Figure S.13, Figure 9 (**Left**) shows that at lower temperatures, *r19* is the most rate-controlling step as the surface is still covered primarily by O_2/O*. As the increasing temperatures increase the reaction rates, *r19* becomes less rate-controlling, and the primary flux-carrying pathway for EO production gradually shifts toward *r16* instead. At sufficiently high temperatures, the production of OMC (*r4*) becomes the most rate-controlling step in an inhibiting manner.

An important observation here is the relationship between the degrees of rate control of the OMC formation step (*r4*) and the Ag_6 pathway (*r16*). An increase in one is accompanied by the corresponding increase in the opposite direction of the other. This coupling is a reflection of the accessibility and site economy of the two types of "free sites". The first type of free site comes in the form of the /O* oxygen vacancy. Gas-phase adsorption steps into the vacancy (*r5, r18*) are equilibrated, and utilization of this site type is unhindered by the occupation of neighboring sites, as *r19* only requires an O_2/O* species, with the C_2H_4 reactant adsorbing directly onto the O_2/O* as was modeled by DFT. The second type of free site is the "free site" in the conventional sense (*). With reactions directly interacting with this free site (*r1*−*r3*) being equilibrated, accessibility to * is represented, in a mean-field sense, by the coverage of O* and O_2* species on the surface. At increasing temperatures, the decreasing coverage of O* and O_2* imparts a kinetic strain on reactions requiring the free site * to proceed. The OMC formation (*r4*) is particularly bottlenecked downstream at *r21*, in which a free site is required for the AA* intermediate to diffuse away from the oxygen vacancy /O* and toward the metallic site * for the combustion

https://doi.org/10.1021/acscatal.4c04521
ACS Catal. 2024, 14, 17880−17892

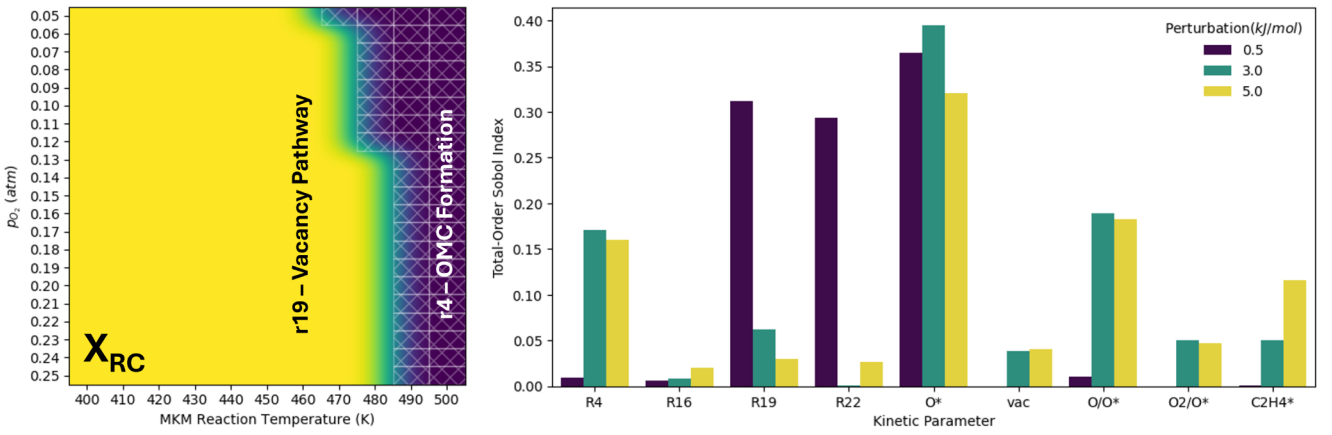

Figure 10. Left: Phase diagram showing which reaction step is the most rate-controlling (based on absolute degree of rate control values). This data set simulates the following conditions: $T = 400-500$ K, $P_{C_2H_4} = 0.25$ atm, $P_{O_2} = 0.05-0.25$ atm, $P_{CO_2} = 0.02$ atm. Total pressure balanced with inert gas to 1 atm. Regions with hatched overlay represent conditions where the most rate-controlling step is controlled via inhibition. **Right**: Total-order Sobol indices of the nine most globally sensitive parameters at three different ranges of parameter perturbation/variance.

steps to proceed. This hurdle is primarily alleviated by *r16* and *r17*, which cumulatively free up multiple free sites *. In this sense, the increasing inhibiting rate control of *r4* must be accompanied by the increasing enhancing rate control of *r16*, by way of the free site economy. The shift to and from the regimes where the populations of the two types of free sites impact the kinetics more significantly are further reflected in Figure 10 (**Left**).

Figure 10 (**Left**) shows how the most rate-controlling reactions change as a function of both reaction temperature and oxygen partial pressure. A more generalized view of the trend seen in Figures 9 and S.13 is observed. At low temperatures with low reactivities, the surface is populated by O_2/O*, and increasing the overall EO TOF hinges upon clearing the catalyst surface of the most abundant species, which is primarily done via *r19*. This limitation persists for most of the lower reaction temperatures of ≤450 K. T = 460−470 K represents the transition region, where the competition between the three main controlling pathways (*r4, r16, r19*) is close enough for the most controlling step to be dependent on the oxygen partial pressure, as seen in Figure 9 (**Left**). At $T \geq 480$ K, the low coverage of O_2/O* is accompanied by a shift in kinetic control *away* from *r19* and toward *r4*. While the OMC formation is most negatively controlling, the degree of rate control of *r16* remains high in this regime due to the previously discussed site balance.

Global Sensitivity Analysis (GSA). The degree of rate control provides a local interpretation of the sensitivity of the TOF with respect to a particular kinetic parameter, i.e., under the assumption that other parameters are static. A variance-based sensitivity analysis can provide a more generally applicable view of how the variance of a particular parameter contributes to the total variance in the output variable. The details of the approach are covered in Section S9. For each parameter perturbation range, 20 000 data points were generated, and the perturbation in each of which was sampled from a uniform random distribution within the set perturbation ranges. For each data set, about 1−3% of the data set encountered convergence or thermodynamic consistency issues, and these data points were discarded.

As seen in Figure 10 (**Right**), at small perturbations (±0.5 kJ/mol) around the nominal point, the most sensitive parameters are qualitatively comparable to the local picture; *r19* is most rate-controlling, and O* is involved either directly with reactions on the metallic phase or indirectly as a reactant for the oxidic reconstruction of the surface. *r22* is particularly interesting, being identified as a kinetically important step. *r22* represents the dissociation of O_2/O*, which can be understood as the interconversion between the two types of free sites.

Extending the perturbation range up to ±5 kJ/mol around the nominal point reveals that the sensitivity of *r19* persists only within a local range of parameter perturbation, whereas O*, as the main reactant, remains important at larger perturbation ranges as well. Moving toward a larger span of the considered parameter space, more distinct parameters are identified as being important, instead of only a handful of important ones (as with the ±0.5 kJ/mol data set). At larger perturbations, all of the oxygen species other than O_2* are identified as being important, as well as both main reactants, represented by O* and C_2H_4*. Interestingly, the OMC formation *r4* is important over a larger range of parameters relative to the two EO flux-carrying pathways *r16* and *r19*. This is a reflection of the different kinds of possible solution types due to the multiple possible pathways for EO generation considered in the model. Some solutions can involve only the Ag_6 pathway (*r16*), only the vacancy pathway (*r19*), or a combination of both. On the other hand, the OMC formation (*r4*) remains important in a more general sense due to its necessity in maintaining the active site economy.

In the context of systematic catalyst design, in a more general sense, the effectiveness of a possible catalyst promoter or promoter combinations can be assessed via their effect on the stability of O*, /O*, O/O*, O_2/O*, and C_2H_4*, as well as how the promoter affects the formation of the OMC intermediate.

CONCLUSION

Following the translation of the known ethylene oxidation mechanism to the partially oxidized Ag surface, a DFT-based exploration of feasible reaction pathways was performed, from which an extended microkinetic model was created. Parameter optimization was performed to ensure that the extended model remains relevant and is able to reproduce experimental observables (E_A, TOF, and reaction orders). The model predicted that not only does the catalyst surface contain a mixed coverage of metallic and oxidized Ag regions but also these coverages change with the change in reaction temperatures

https://doi.org/10.1021/acscatal.4c04521
ACS Catal. 2024, 14, 17880−17892

and reactant partial pressures. Said changes in the oxidized extent of the surface are also correlated with changes in reaction kinetics, the most notable being higher temperatures shifting the kinetic choke point away from the direct ethylene oxidation by O_2/O* and toward the site balance interplay between the formation of the OMC intermediate and ethylene oxidation via O/Ag_6. While the oxidation of ethylene via O_2/O* controls the reaction rate, especially at lower temperatures, within a broader range of the design space of the system, the EO TOF was found to be more sensitive to the formation of the OMC intermediate as well as the binding strength of the different oxygen-based species and the adsorbed ethylene intermediate. In line with our previous Raman study,[33] the extended MKM identified the O_2/O* species as the most active species for EO production, here, maintaining high fluxes through *r16* and *r19*.

It is important to reiterate that the p(4 × 4)-O-Ag(111) reconstruction is chosen as a *model* catalyst for its relatively ordered nature, stability, the Ag_2O stoichiometry for the top atomic layer, and because it allows for the stable formation of oxygen vacancies along with its associated atomic and diatomic oxygen species both on the adsorbate layer and below the topmost Ag layer. In the fluctuating conditions of the oxidation reaction, and in consideration of the many other similarly stable reconstructions of the Ag catalyst, it is likely that the oxidic coverage of the Ag catalyst is composed of many slightly different configurations of partially oxidized Ag. However, the focus of this study is on the kinetic and mechanistic role of a diatomic oxygen intermediate that occupies a site previously occupied by an atomic "lattice" oxygen, i.e., an oxygen vacancy. This dioxygen species in the vacancy site was previously reported as the active species in ethylene oxidation and has been reported in other oxidic reconstructions/oxidized forms of the Ag catalyst as well. It should be noted that this type of dioxygen species is distinct from the surface-level dioxygen adsorbate O_2*, which was the center point of the discussions in the ethylene oxidation literature from decades past.

Although notions of a nonmetallic catalyst surface and hybrid oxygen species have been in discussions, especially in the past few years of ethylene oxidation literature, the current DFT−MKM study would like to encourage a shift in the collective mechanistic understanding of the reaction system. With this extended reaction network as a foundation, investigations, particularly regarding promoter effects, can be performed at a higher mechanistic resolution.

■ ASSOCIATED CONTENT

Supporting Information

The Supporting Information is available free of charge at https://pubs.acs.org/doi/10.1021/acscatal.4c04521.

Microkinetic modeling (MKM) formulation, parameter optimization formulation, multistart optimization procedure, ensemble-scale statistics from the multistart optimization, extended discussions on the activation of ethylene (C_2H_4) double bond via a singlet oxygen, competing pathways for acetaldehyde (AA) formation, optimized MKM parameters, formulation of local and global sensitivity analyses, charge analysis results, supplemental plots (including structural diagrams, potential energy diagrams, and density of states plots), and additional vibrational frequency calculation results (PDF)

MKM code written in the Python language (ZIP)

■ AUTHOR INFORMATION

Corresponding Authors

Israel E. Wachs − *Department of Chemical and Biomolecular Engineering, Lehigh University, Bethlehem, Pennsylvania 18015, United States;* orcid.org/0000-0001-5282-128X; Email: iew0@lehigh.edu

Srinivas Rangarajan − *Department of Chemical and Biomolecular Engineering, Lehigh University, Bethlehem, Pennsylvania 18015, United States;* orcid.org/0000-0002-6777-9421; Email: srr516@lehigh.edu

Authors

Adhika Setiawan − *Department of Chemical and Biomolecular Engineering, Lehigh University, Bethlehem, Pennsylvania 18015, United States;* orcid.org/0000-0001-7908-6473

Tiancheng Pu − *Department of Chemical and Biomolecular Engineering, Lehigh University, Bethlehem, Pennsylvania 18015, United States;* orcid.org/0000-0002-4775-4294

Complete contact information is available at: https://pubs.acs.org/10.1021/acscatal.4c04521

Notes

The authors declare no competing financial interest.

■ ACKNOWLEDGMENTS

This material is based upon work supported by the National Science Foundation (NSF) under grants #1804104 and #2045550. This study was conducted on Lehigh University's Research Computing infrastructure, partially supported by NSF grant #2019035, as well as Expanse at the San Diego Supercomputer Center (SDSC) and Stampede2 at Texas Advanced Computing Center through allocation CTS170035 from the Advanced Cyberinfrastructure Coordination Ecosystem: Services & Support (ACCESS) program,[77] which is supported by NSF grants #2138259, #2138286, #2138307, #2137603, and #2138296. We would like to acknowledge Dr. Huijie Tian for the guidance and help with setting up the general optimization workflow.

■ REFERENCES

(1) Hess, C.; Schlögl, R. *Nanostructured Catalysts: Selective Oxidations*; Royal Society of Chemistry: 2011, p 6HEoDwAAQBAJ.

(2) *Ethylene Oxide Market | 2022 - 27 | Industry Share, Size, Growth - Mordor Intelligence*. 2022, https://www.mordorintelligence.com/industry-reports/ethylene-oxide-market.

(3) Pu, T.; Tian, H.; Ford, M. E.; Rangarajan, S.; Wachs, I. E. Overview of Selective Oxidation of Ethylene to Ethylene Oxide by Ag Catalysts. *ACS Catal.* **2019**, *9*, 10727−10750.

(4) Grant, R. B.; Lambert, R. M. Basic studies of the oxygen surface chemistry of silver: Chemisorbed atomic and molecular species on pure Ag(111). *Surf. Sci.* **1984**, *146*, 256−268.

(5) Grant, R. B.; Lambert, R. M. A single crystal study of the silver-catalysed selective oxidation and total oxidation of ethylene. *J. Catal.* **1985**, *92*, 364−375.

(6) Linic, S.; Barteau, M. A. Formation of a Stable Surface Oxametallacycle that Produces Ethylene Oxide. *J. Am. Chem. Soc.* **2002**, *124*, 310−317.

(7) Jones, G. S.; Mavrikakis, M.; Barteau, M. A.; Vohs, J. M. First Synthesis, Experimental and Theoretical Vibrational Spectra of an Oxametallacycle on a Metal Surface. *J. Am. Chem. Soc.* **1998**, *120*, 3196−3204.

(8) Christopher, P.; Linic, S. Engineering Selectivity in Heterogeneous Catalysis: Ag Nanowires as Selective Ethylene Epoxidation Catalysts. *J. Am. Chem. Soc.* **2008**, *130*, 11264−11265.

(9) Huš, M.; Hellman, A. Ethylene Epoxidation on Ag(100), Ag(110), and Ag(111): A Joint Ab Initio and Kinetic Monte Carlo Study and Comparison with Experiments. *ACS Catal.* **2019**, *9*, 1183−1196.
(10) Linic, S.; Barteau, M. A. Control of Ethylene Epoxidation Selectivity by Surface Oxametallacycles. *J. Am. Chem. Soc.* **2003**, *125*, 4034−4035.
(11) Ozbek, M. O.; Onal, I.; van Santen, R. A. Effect of Surface and Oxygen Coverage on Ethylene Epoxidation. *Top. Catal.* **2012**, *55*, 710−717.
(12) Linic, S.; Barteau, M. A. Construction of a reaction coordinate and a microkinetic model for ethylene epoxidation on silver from DFT calculations and surface science experiments. *J. Catal.* **2003**, *214*, 200−212.
(13) Zhu, L.; Zhang, W.; Zhu, J.; Cheng, D. Mechanistic insight into the facet-dependent selectivity of ethylene epoxidation on Ag nanocatalysts. *Appl. Catal., A* **2017**, *538*, 27−36.
(14) Chen, C.-J.; Harris, J. W.; Bhan, A. Kinetics of Ethylene Epoxidation on a Promoted Ag/α-Al2O3 Catalyst−The Effects of Product and Chloride Co-Feeds on Rates and Selectivity. *Chem.− A Eur. J.* **2018**, *24*, 12405−12415.
(15) Dettwiler, H. R.; Baiker, A.; Richarz, W. Kinetics of Ethylene Oxidation on a Supported Silver Catalyst. *Helv. Chim. Acta* **1979**, *62*, 1689−1700.
(16) Kenson, R. E.; Lapkin, M. Kinetics and mechanism of ethylene oxidation. Reactions of ethylene and ethylene oxide on a silver catalyst. *J. Phys. Chem.* **1970**, *74*, 1493−1502.
(17) Stegelmann, C.; Schiødt, N.; Campbell, C.; Stoltze, P. Microkinetic modeling of ethylene oxidation over silver. *J. Catal.* **2004**, *221*, 630−649.
(18) Li, W.-X.; Stampfl, C.; Scheffler, M. Subsurface oxygen and surface oxide formation at Ag(111): A density-functional theory investigation. *Phys. Rev. B* **2003**, *67*, 045408.
(19) Schnadt, J.; Knudsen, J.; Hu, X. L.; Michaelides, A.; Vang, R. T.; Reuter, K.; Li, Z.; Lægsgaard, E.; Scheffler, M.; Besenbacher, F. Experimental and theoretical study of oxygen adsorption structures on Ag(111). *Phys. Rev. B* **2009**, *80*, 075424.
(20) Schnadt, J.; Michaelides, A.; Knudsen, J.; Vang, R. T.; Reuter, K.; Lægsgaard, E.; Scheffler, M.; Besenbacher, F. Revisiting the Structure of the p(4 × 4) Surface Oxide on Ag(111). *Phys. Rev. Lett.* **2006**, *96*, 146101.
(21) Pu, T.; Setiawan, A.; Mosevitzky Lis, B.; Zhu, M.; Ford, M. E.; Rangarajan, S.; Wachs, I. E. Nature and Reactivity of Oxygen Species on/in Silver Catalysts during Ethylene Oxidation. *ACS Catal.* **2022**, *12*, 4375−4381.
(22) Andryushechkin, B. V.; Shevlyuga, V. M.; Pavlova, T. V.; Zhidomirov, G. M.; Eltsov, K. N. Adsorption of molecular oxygen on the Ag(111) surface: A combined temperature-programmed desorption and scanning tunneling microscopy study. *J. Chem. Phys.* **2018**, *148* (24), 244702.
(23) Pai, W. W.; Reutt-Robey, J. E. Formation of (n × 1)-O/Ag(110) overlayers and the role of step-edge atoms. *Phys. Rev. B* **1996**, *53*, 15997−16005.
(24) Xu, Y.; Greeley, J.; Mavrikakis, M. Effect of Subsurface Oxygen on the Reactivity of the Ag(111) Surface. *J. Am. Chem. Soc.* **2005**, *127*, 12823−12827.
(25) Özbek, M. O.; van Santen, R. A. The Mechanism of Ethylene Epoxidation Catalysis. *Catal. Lett.* **2013**, *143*, 131−141.
(26) Özbek, M. O.; Onal, I.; van Santen, R. A. Why silver is the unique catalyst for ethylene epoxidation. *J. Catal.* **2011**, *284*, 230−235.
(27) Tang, Z.; Chen, T.; Liu, K.; Du, H.; Podkolzin, S. G. Atomic, Molecular and Hybrid Oxygen Structures on Silver. *Langmuir* **2021**, *37*, 11603−11610.
(28) Liu, C.; Wijewardena, D. P.; Sviripa, A.; Sampath, A.; Flaherty, D. W.; Paolucci, C. Computational and experimental insights into reactive forms of oxygen species on dynamic Ag surfaces under ethylene epoxidation conditions. *J. Catal.* **2022**, *405*, 445−461.
(29) Özbek, M. O.; Onal, I.; Santen Van, R. A. Ethylene epoxidation catalyzed by chlorine-promoted silver oxide. *J. Phys.: condens. Matter* **2011**, *23* (40), 404202.
(30) Jones, T. E.; Wyrwich, R.; Böcklein, S.; Rocha, T. C. R.; Carbonio, E. A.; Knop-Gericke, A.; Schlögl, R.; Günther, S.; Wintterlin, J.; Piccinin, S. Oxidation of Ethylene on Oxygen Reconstructed Silver Surfaces. *J. Phys. Chem. C* **2016**, *120*, 28630−28638.
(31) Harris, J. W.; Wang, L.; DeWilde, J. F. Kinetic Modeling of Ethylene Epoxidation Kinetics as a Function of Chlorine Coverage over a Highly Promoted Silver Catalyst. *Ind. Eng. Chem. Res.* **2019**, *58*, 19061−19071.
(32) Liu, J.-X.; Lu, S.; Ann, S.-B.; Linic, S. Mechanisms of Ethylene Epoxidation over Silver from Machine Learning-Accelerated First-Principles Modeling and Microkinetic Simulations. *ACS Catal.* **2023**, *13*, 8955−8962.
(33) Pu, T.; Setiawan, A.; Foucher, A. C.; Guo, M.; Jehng, J.-M.; Zhu, M.; Ford, M. E.; Stach, E. A.; Rangarajan, S.; Wachs, I. E. Revealing the Nature of Active Oxygen Species and Reaction Mechanism of Ethylene Epoxidation by Supported Ag/α-Al2O3 Catalysts. *ACS Catal.* **2024**, *14*, 406−417.
(34) Kresse, G.; Hafner, J. Ab initio molecular dynamics for liquid metals. *Phys. Rev. B* **1993**, *47*, 558−561.
(35) Kresse, G.; Hafner, J. Ab initio molecular-dynamics simulation of the liquid-metal−amorphous-semiconductor transition in germanium. *Phys. Rev. B* **1994**, *49*, 14251−14269.
(36) Kresse, G.; Furthmüller, J. Efficiency of ab-initio total energy calculations for metals and semiconductors using a plane-wave basis set. *Comput. Mater. Sci.* **1996**, *6*, 15−50.
(37) Kresse, G.; Furthmüller, J. Efficient iterative schemes for ab initio total-energy calculations using a plane-wave basis set. *Phys. Rev. B* **1996**, *54*, 11169−11186.
(38) Perdew, J. P.; Burke, K.; Ernzerhof, M. Generalized Gradient Approximation Made Simple. *Phys. Rev. Lett.* **1996**, *77*, 3865−3868.
(39) Becke, A. D.; Johnson, E. R. Exchange-hole dipole moment and the dispersion interaction: High-order dispersion coefficients. *J. Chem. Phys.* **2006**, *124* (1), 014104.
(40) Steinmann, S. N.; Corminboeuf, C. Comprehensive Benchmarking of a Density-Dependent Dispersion Correction. *J. Chem. Theory Comput.* **2011**, *7*, 3567−3577.
(41) Steinmann, S. N.; Corminboeuf, C. A generalized-gradient approximation exchange hole model for dispersion coefficients. *J. Chem. Phys.* **2011**, *134* (4), 044117.
(42) Jónsson, H.; Mills, G.; Jacobsen, K. W. *Classical and Quantum Dynamics in Condensed Phase Simulations*; World scientific, 1998; pp. 385−404.
(43) Mills, G.; Jónsson, H. Quantum and thermal effects in ${\mathrm{H}}_{2}$ dissociative adsorption: Evaluation of free energy barriers in multidimensional quantum systems. *Phys. Rev. Lett.* **1994**, *72*, 1124−1127.
(44) Mills, G.; Jónsson, H.; Schenter, G. K. Reversible work transition state theory: application to dissociative adsorption of hydrogen. *Surf. Sci.* **1995**, *324*, 305−337.
(45) Henkelman, G.; Uberuaga, B. P.; Jónsson, H. A climbing image nudged elastic band method for finding saddle points and minimum energy paths. *J. Chem. Phys.* **2000**, *113*, 9901−9904.
(46) Henkelman, G.; Jónsson, H. Improved tangent estimate in the nudged elastic band method for finding minimum energy paths and saddle points. *J. Chem. Phys.* **2000**, *113*, 9978−9985.
(47) Hindmarsh, A. C.; Brown, P. N.; Grant, K. E.; Lee, S. L.; Serban, R.; Shumaker, D. E.; Woodward, C. S. SUNDIALS: Suite of nonlinear and differential/algebraic equation solvers. *ACM Trans. Math. Software* **2005**, *31*, 363−396.
(48) Gardner, D. J.; Reynolds, D. R.; Woodward, C. S.; Balos, C. J. Enabling New Flexibility in the SUNDIALS Suite of Nonlinear and Differential/Algebraic Equation Solvers. *ACM Trans. Math. Softw* **2022**, *48* (3), 1−24.
(49) Bhandari, S.; Rangarajan, S.; Mavrikakis, M. Combining Computational Modeling with Reaction Kinetics Experiments for Elucidating the In Situ Nature of the Active Site in Catalysis. *Acc. Chem. Res.* **2020**, *53*, 1893−1904.

https://doi.org/10.1021/acscatal.4c04521
ACS Catal. 2024, 14, 17880−17892

(50) Chen, J.; Jia, M.; Hu, P.; Wang, H. CATKINAS: A large-scale catalytic microkinetic analysis software for mechanism auto-analysis and catalyst screening. *J. Comput. Chem.* **2021**, *42*, 379−391.
(51) Xie, W.; Xu, J.; Chen, J.; Wang, H.; Hu, P. Achieving Theory−Experiment Parity for Activity and Selectivity in Heterogeneous Catalysis Using Microkinetic Modeling. *Acc. Chem. Res.* **2022**, *55*, 1237−1248.
(52) Shao, Z.-J.; Zhang, L.; Liu, H.; Cao, X.-M.; Hu, P. Enhanced Interfacial H2 Activation for Nitrostyrene Catalytic Hydrogenation over Rutile Titania-Supported Gold by Coadsorption: A First-Principles Microkinetic Simulation Study. *ACS Catal.* **2019**, *9*, 11288−11301.
(53) Chen, J.-F.; Mao, Y.; Wang, H.-F.; Hu, P. Reversibility Iteration Method for Understanding Reaction Networks and for Solving Microkinetics in Heterogeneous Catalysis. *ACS Catal.* **2016**, *6*, 7078−7087.
(54) Wächter, A.; Biegler, L. T. On the implementation of an interior-point filter line-search algorithm for large-scale nonlinear programming. *Math. Program.* **2006**, *106*, 25−57.
(55) Andersson, J. A. E.; Gillis, J.; Horn, G.; Rawlings, J. B.; Diehl, M. CasADi: a software framework for nonlinear optimization and optimal control. *Math. Program. Comput.* **2019**, *11*, 1−36.
(56) Mhadeshwar, A. B.; Wang, H.; Vlachos, D. G. Thermodynamic Consistency in Microkinetic Development of Surface Reaction Mechanisms. *J. Phys. Chem. B* **2003**, *107*, 12721−12733.
(57) Jones, T. E.; Rocha, T. C. R.; Knop-Gericke, A.; Stampfl, C.; Schlögl, R.; Piccinin, S. Thermodynamic and spectroscopic properties of oxygen on silver under an oxygen atmosphere. *Phys. Chem. Chem. Phys.* **2015**, *17*, 9288−9312.
(58) Guo, M.; Dongfang, N.; Iannuzzi, M.; van Bokhoven, J. A.; Artiglia, L. Structure and Reactivity of Active Oxygen Species on Silver Surfaces for Ethylene Epoxidation. *ACS Catal.* **2024**, *14*, 10234−10244.
(59) Bukhtiyarov, V. I.; Prosvirin, I. P.; Kvon, R. I. Study of reactivity of oxygen states adsorbed at a silver surface towards C2H4 by XPS, TPD and TPR. *Surf. Sci.* **1994**, *320*, L47−L50.
(60) Henriques, C.; Portela, M. F.; Mazzocchia, C. A temperature programmed surface reaction study of the catalytic epoxidation and total oxidation of ethylene on silver. *Stud. Surf. Sci. Catal.* **1994**, *82*, 499−506.
(61) Bal'zhinimaev, B. S. Ethylene epoxidation over silver catalysts. *Kinet. Catal.* **1999**, *40*, 795−810.
(62) Chen, D.; Shang, C.; Liu, Z.-P. Machine-learning atomic simulation for heterogeneous catalysis. *Npj Comput. Mater.* **2023**, *9* (1), 2.
(63) Jankowiak, J. T.; Barteau, M. A. Ethylene epoxidation over silver and copper−silver bimetallic catalysts: I. Kinetics and selectivity. *J. Catal.* **2005**, *236*, 366−378.
(64) Ren, D.; Xu, H.; Li, J.; Li, J.; Cheng, D. Origin of enhanced ethylene oxide selectivity by Cs-promoted silver catalyst. *Mol. Catal.* **2017**, *441*, 92−99.
(65) Ren, D.; Cheng, G.; Li, J.; Li, J.; Dai, W.; Sun, X.; Cheng, D. Effect of Rhenium Loading Sequence on Selectivity of Ag−Cs Catalyst for Ethylene Epoxidation. *Catal. Lett.* **2017**, *147*, 2920−2928.
(66) Prabhakaran, K.; Rao, C. N. R. A combined EELS-XPS study of molecularly chemisorbed oxygen on silver surfaces: Evidence for superoxo and peroxo species. *Surface Science Letters* **1987**, *186*, 575−580.
(67) Kondarides, D. I.; Papatheodorou, G. N.; Vayenas, C. G.; Verykios, X. E. In Situ High Temperature SERS Study of Oxygen Adsorbed on Ag: Support and Electrochemical Promotion Effects. *Ber. Bunsenges. Phys. Chem.* **1993**, *97*, 709−719.
(68) J. Millar, G.; B. Metson, J.; A. Bowmaker, G.; P. Cooney, R. In situ Raman studies of the selective oxidation of methanol to formaldehyde and ethene to ethylene oxide on a polycrystalline silver catalyst. *Faraday Trans.* **1995**, *91* (22), 4149−4159.
(69) Bao, X.; Pettinger, B.; Ertl, G.; Schlögl, R. In-situ Raman Studies of Ethylene Oxidation at Ag(111) and Ag(110) under Catalytic Reaction Conditions. *Ber. Bunsenges. Phys. Chem.* **1993**, *97*, 322−325.
(70) Li, W.-X.; Stampfl, C.; Scheffler, M. Why is a Noble Metal Catalytically Active? The Role of the O-Ag Interaction in the Function of Silver as an Oxidation Catalyst. *Phys. Rev. Lett.* **2003**, *90*, 256102.
(71) Pettenkofer, C.; Pockrand, I.; Otto, A. Surface enhanced Raman spectra of oxygen adsorbed on silver. *Surf. Sci.* **1983**, *135*, 52−64.
(72) Nair, A.; Joshi, K. What leads to direct epoxidation? An exhaustive DFT investigation of electrophilic oxygen mediated epoxidation of ethylene on Ag(100). *Comput. Mater. Sci.* **2024**, *239*, 112959.
(73) Chen, D.; Chen, L.; Zhao, Q.-C.; Yang, Z.-X.; Shang, C.; Liu, Z.-P. Square-pyramidal subsurface oxygen [Ag4OAg] drives selective ethene epoxidation on silver. *Nat. Catal.* **2024**, *7*, 536−545.
(74) Chen, D.; Kang, P.-L.; Liu, Z.-P. Active Site of Catalytic Ethene Epoxidation: Machine-Learning Global Pathway Sampling Rules Out the Metal Sites. *ACS Catal.* **2021**, *11*, 8317−8326.
(75) Egelske, B. T.; Xiong, W.; Zhou, H.; Monnier, J. R. Effects of the method of active site characterization for determining structure-sensitivity in Ag-catalyzed ethylene epoxidation. *J. Catal.* **2022**, *410*, 221−235.
(76) Campbell, C. T. Atomic and molecular oxygen adsorption on Ag(111). *Surf. Sci.* **1985**, *157*, 43−60.
(77) Boerner, T. J.; Deems, S.; Furlani, T. R.; Knuth, S. L.; Towns, J. *ACCESS: Advancing Innovation: nSF's Advanced Cyberinfrastructure Coordination Ecosystem: services & Support*; Practice and Experience in Advanced Research Computing.: New York, NY, USA, 2023; pp. 173−176.

https://doi.org/10.1021/acscatal.4c04521
ACS Catal. 2024, 14, 17880−17892